PHYSICAL REVIEW B **105**, 235119 (2022)

Large intrinsic spin Hall conductivity and spin Hall angle in the nodal-line semimetals $ThAl_2$ and $ThGa_2$

Ning-Ning Zhao, Kai Liu,[*] and Zhong-Yi Lu[†]
Department of Physics and Beijing Key Laboratory of Opto-electronic Functional Materials & Micro-nano Devices, Renmin University of China, Beijing 100872, China

(Received 26 February 2022; revised 28 April 2022; accepted 2 June 2022; published 15 June 2022)

The intrinsic spin Hall effect and topological properties of $ThAl_2$ and $ThGa_2$ have been investigated based on first-principles electronic structure calculations. The band structures calculated without the spin-orbital coupling (SOC) show that both $ThAl_2$ and $ThGa_2$ host multiple nodal lines near the Fermi level. Once the SOC is taken into account, these nodal lines are gapped and huge spin Berry curvatures can be generated. As a result, giant spin Hall conductances of $ThAl_2$ and $ThGa_2$ are induced around the Fermi level. Moreover, large spin Hall angles can be achieved due to the giant spin Hall conductance and the small electric conductivity. Our work indicates that $ThAl_2$ and $ThGa_2$ not only provide an ideal platform for exploring the interplay between spin Hall effect and topological property, but also have promising applications in spin-orbitronic devices.

DOI: 10.1103/PhysRevB.105.235119

I. INTRODUCTION

The spin Hall effect (SHE) is a fascinating electronic transport property analogous to the anomalous Hall effect (AHE) [1–3]. In the SHE, a transverse pure spin current with spin-polarization perpendicular to the plane defined by the charge and spin currents is generated by the longitudinal charge current. Different from the AHE, a nonzero magnetic moment is not needed for the SHE [4]. Importantly, a spin-orbital torque can be induced via the SHE, which is used to manipulate the magnetization without external magnetic field [5,6]. To account for the SHE in a material, two types of mechanisms have been proposed, which are the extrinsic mechanism and the intrinsic mechanism borrowed directly from the AHE. The extrinsic mechanism refers to a spin acquires a transverse velocity from the spin skew scattering or side jump scattering due to the spin-orbital coupling (SOC) effect, while the intrinsic mechanism depends only on the band structure of a perfect crystal [2,7,8]. Thus, the intrinsic spin Hall conductance (SHC) can be accurately calculated by integrating the spin Berry curvature (SBC) of the occupied bands in the Brillouin zone (BZ), in analogy with the ordinary Berry curvature (BC) [9–12].

In addition to the SHC, the spin Hall angle (SHA) measures the efficiency of a charge-spin current conversion, which is defined by the ratio of the SHC to the electric conductivity [13]. Due to the spin-momentum-locked surface states, topological insulators are considered to be ideal materials for generating a pure spin current with a large SHA, however, the bulk channels enhanced at room temperature may diminish the signals of spin orbit torques derived from surface states [14–17]. On the other hand, the heavy metal Pt shows a remarkably large SHC ($\sim 2000\hbar/\mathrm{e}$) but a low SHA due to the high electric conductivity [18,19]. Recently, Weyl semimetals such as TaAs have been predicted to host a large intrinsic SHC resulting from the Weyl nodes [20,21]. Furthermore, a recent high-throughput calculation on the SHC in >20 000 nonmagnetic materials indicates that the large SHC is closely associated with the nodal lines protected by the mirror symmetry [22]. Similar to an ordinary BC, a large SBC can be created around a Weyl node or a gapped nodal line in topological semimetals, then resulting in a large SHC [23–32]. In addition, a relatively low electric conductivity in semimetals can enhance an SHA [33]. To study the interplay between the SHC and the band topology as well as to design new devices for spin-charge current conversion, it is important to search for more topological semimetals with large intrinsic SHC and SHA.

Based on first-principles electronic structure calculations, in this work we propose that the AlB_2-type Th-based intermetallics $ThAl_2$ and $ThGa_2$ are a new class of topological semimetals with large intrinsic SHC, which originates from the multiple nodal lines. In particular, due to the high resistivity reported in a previous experiment [34], $ThAl_2$ and $ThGa_2$ exhibit significant SHA values. Our calculations thus demonstrate a promising material platform for realizing large SHC and SHA.

II. METHOD

The electronic structures and the transport properties of $ThAl_2$ and $ThGa_2$ were studied by using the density functional theory [35,36] calculations as implemented in the Quantum ESPRESSO package [37]. A plane-wave basis was used, and the ultrasoft and projector augmented wave pseudopotentials were adopted from PSLIBRARY [38,39]. The valence configurations of Th atom and Al atom we used were $6s^2 6p^6 5f^1 6d^1 7s^2$ and $3s^2 3p^1$, respectively. For the exchange

---

[*] kliu@ruc.edu.cn
[†] zlu@ruc.edu.cn

and correlation functional, the generalized gradient approximation of Perdew-Burke-Ernzerhof type [40] was adopted. The kinetic energy cutoff of the plane-wave basis was set to be 135 Ry. A $14 \times 14 \times 14$ **k**-point mesh was used for the BZ sampling and the Gaussian smearing method with a width of 0.004 Ry was adopted for the Fermi surface broadening. In the structural optimization, both lattice constants and internal atomic positions were fully relaxed until the forces on all the atoms were smaller than 0.0002 Ry/bohr. The SOC effect was taken into account in the calculations of electronic structures. In order to explore the SHC and the SHA, the tight-binding Hamiltonian was constructed with the maximally localized Wannier functions [41,42] for the outermost s, p, d and f orbitals of Th atoms and the outermost s, p orbitals of Al and Ga atoms generated by the first-principles calculations. Based on the Wannier-interpolation approach, the SHC and the SBC were evaluated via the Kubo-formula approach in the linear response scheme as follows [9,10,12]:

$$\sigma_{xy}^{z} = -\frac{e^2}{\hbar}\frac{1}{VN_k}\sum_{n}\sum_{\mathbf{k}} f_{n\mathbf{k}}\Omega_{n,xy}^{z}(\mathbf{k}), \tag{1}$$

$$\Omega_{xy}^{z}(\mathbf{k}) = \sum_{n} f_{n\mathbf{k}}\Omega_{n,xy}^{z}(\mathbf{k}), \tag{2}$$

$$\Omega_{n,xy}^{z}(\mathbf{k}) = \hbar\sum_{m\neq n}\frac{-2\,\mathrm{Im}\,\langle n\mathbf{k}|\,\hat{j}_x^z\,|m\mathbf{k}\rangle\,\langle m\mathbf{k}|\,\hat{v}_y\,|n\mathbf{k}\rangle}{(\epsilon_{n\mathbf{k}}-\epsilon_{m\mathbf{k}})^2+\eta^2}, \tag{3}$$

where $f_n(\mathbf{k})$ is the Fermi-Dirac distribution function, n is the band index, $\epsilon_{n\mathbf{k}}$ is the eigenvalue of the nth eigenstate $|n\mathbf{k}\rangle$, V is the primitive cell volume, N_k is the number of k points in sampling the BZ, and η is a small quantity to avoid numerical divergence. The $\hat{j}_x^z = \frac{1}{2}\{\hat{s}_z, \hat{v}_x\}$ is the spin current operator with the $\hat{s}_z = \frac{\hbar}{2}\hat{\sigma}_z$ being the spin operator and the $\hat{v}_i = \frac{1}{\hbar}\frac{\partial H(\mathbf{k})}{\partial \mathbf{k}_i} (i = x, y, z)$ being the velocity operator. Here $\Omega_{n,xy}^{z}(\mathbf{k})$ is the band-projected spin Berry curvature and $\Omega_{xy}^{z}(\mathbf{k})$ is the **k**-resolved term by integrating the spin Berry curvature of the occupied bands. The SHC is a third-order tensor and the element σ_{xy}^{z} represents that the spin current along the x direction is induced by the electric field along the y direction, where the spin current is polarized along the z direction. A **k**-point grid of $100 \times 100 \times 100$ for the Wannier interpolation and the adaptive refinement **k** mesh of $4 \times 4 \times 4$ were used in the integral calculation.

In order to evaluate the SHA, the electric conductivity tensor was calculated based on the Boltzmann transport equations within the constant relaxation time approximation as follows [43]:

$$[\sigma]_{ij}(\mu, T) = e^2\int_{-\infty}^{\infty} dE\left(-\frac{\partial f(E,\mu,T)}{\partial E}\right)\Sigma_{ij}(E), \tag{4}$$

$$\Sigma_{ij}(E) = \frac{1}{V}\sum_{n,\mathbf{k}} v_i(n,\mathbf{k})v_j(n,\mathbf{k})\tau_{n,\mathbf{k}}\delta(E - E_{n,\mathbf{k}}), \tag{5}$$

where μ is the chemical potential, $\Sigma_{ij}(E)$ is the transport distribution function, $\tau_{n,\mathbf{k}}$ is the relaxation time depending on the band and the wave vector, which describes the collisional term in the Boltzmann equation. In the calculation, we assumed that the lifetime $\tau_{n,\mathbf{k}}$ is independent of both n and **k** and chose the value $\tau = \tau_{n,\mathbf{k}}$ by fitting the experimental electric conductivity at a given temperature.

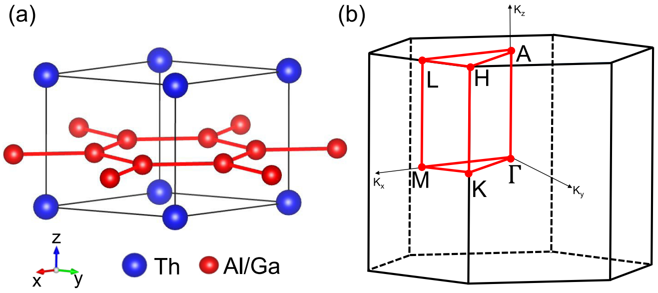

FIG. 1. (a) Crystal structure and (b) Bulk Brillouin zone (BZ) of the AlB_2-type $ThAl_2$ and $ThGa_2$. The red lines indicate the high-symmetry paths in the BZ.

III. RESULTS

The thorium intermetallic compounds $ThAl_2$ and $ThGa_2$ crystalize in the AlB_2-type hexagonal structure with space group P6/*mmm* (No. 191). From the crystal structure shown in Fig. 1(a), we can see that Al (Ga) atoms form the AA-stacking flat layers with a honeycomb lattice, while Th atoms occupy the interlayer positions above the centers of the hexagons. The calculated lattice constants are $a = 4.42$ Å and $c = 4.15$ Å for $ThAl_2$, and $a = 4.27$ Å and $c = 4.25$ Å for $ThGa_2$, which agree well with their experimental values [44]. The corresponding bulk BZ along with the high-symmetry **k** points is shown in Fig. 1(b).

Figures 2(a) and 2(b) show the electronic band structures of $ThAl_2$ along the high-symmetry paths of the BZ calculated without and with the inclusion of SOC, respectively. As shown in Fig. 2(a), there are two bands crossing the Fermi level with large dispersion, which form a carousel-like Fermi surface displayed in Fig. 2(d). According to the calculated density of states (DOS) [Fig. 2(c)], the Th 6*d* orbitals have more

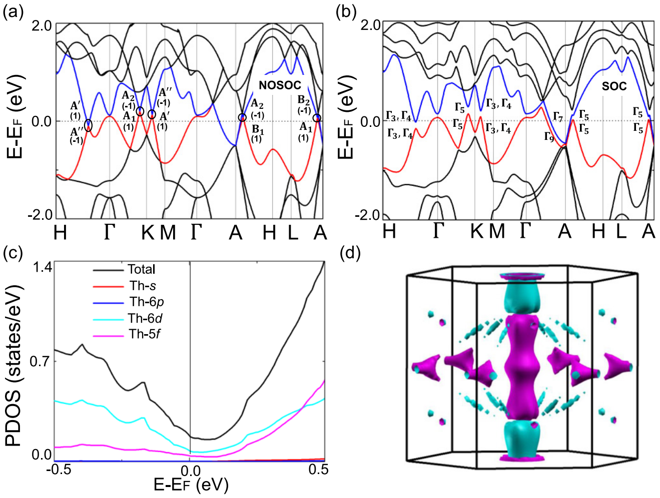

FIG. 2. Electronic band structures of $ThAl_2$ calculated (a) without and (b) with the spin-orbital coupling (SOC) along the high-symmetry paths of the BZ. The red and blue lines indicate the highest valence band and the lowest conduction band, respectively. The mirror parities of the crossing bands at the gapless points are also labeled.(c) Total and partial density of states calculated without the SOC. (d) Fermi surface of $ThAl_2$ calculated without the SOC.

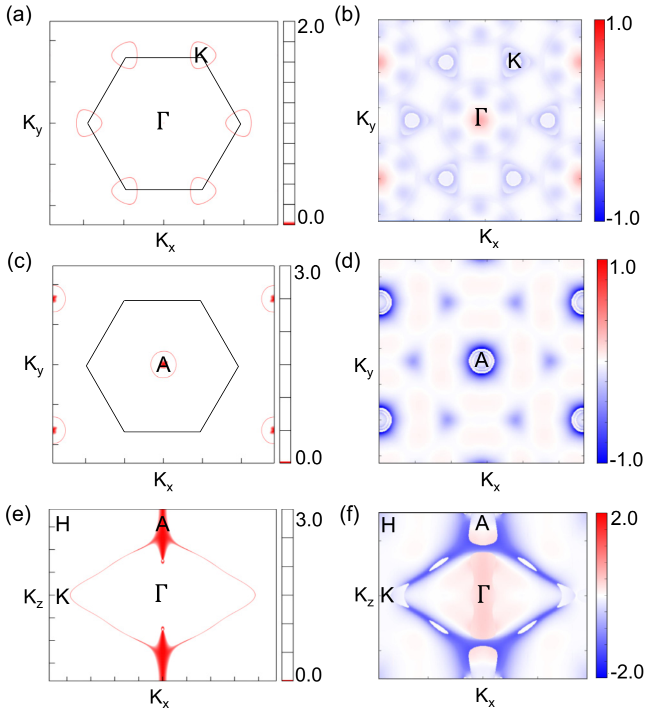

FIG. 3. The nodal lines of ThAl$_2$ formed between the highest valence band and the lowest conduction band at the (a) $k_z = 0$, (c) $k_z = \pi$, and (e) $k_x = 0$ planes. The red lines represent the spinless nodal lines without the SOC. The calculated **k**-resolved spin Berry curvatures $\Omega^z_{xy}(\mathbf{k})$ on a log scale with the inclusion of SOC, respectively, in the corresponding (b) $k_z = 0$, (d) $k_z = \pi$, and (f) $k_x = 0$ planes at the Fermi level E_f. The red and blue colors indicate the positive and negative values of the spin Berry curvature, respectively.

contributions around the Fermi level than the Th $5f$ orbitals, making Th atom behave like a transition metal. In addition, the small DOS at the Fermi level results in a low conductivity, which is discussed later.

From the band structure calculated without the inclusion of SOC [Fig. 2(a)], there are several linear band crossings between the highest valence band (red band) and the lowest conduction band (blue band) near the Fermi level as highlighted by the black circles, indicating that they may be nodal lines in the BZ. Along the H-Γ and Γ-K paths, the nodal points are formed by the singlet A' and A'' states of $\mathcal{C}_s$ point group and the singlet A_2 and A_1 states of $\mathcal{C}_{2v}$ point group, respectively. At the gapless points, the two bands have the opposite eigenvalues 1 and -1 of mirror operator. Therefore, these band crossings are protected by the σ_v mirror symmetry [45,46]. By checking the energy gap between the valence band and the conduction band on the $k_x = 0$ plane, we find that the nodal points form a continuous nodal ring around the Γ point [Fig. 3(e)]. Likewise, the crossings along the Γ-K-M path and the L-A-H path are both protected by the σ_h mirror reflection symmetry. Thus, the k points with zero energy gap between the valence and conduction bands also form nodal rings on the $k_z = 0$ plane [Fig. 3(a)] and the $k_z = \pi$ plane [Fig. 3(b)], respectively. In addition, along the Γ-A path, a straight degenerate nodal line formed by the E_1 doublet state of the $\mathcal{C}_{6v}$ point group can also be observed [Fig. 3(e)]. Interestingly, the two nodal rings around the K point on the $k_z = 0$ plane and around the Γ point on the $k_x = 0$ planes share the same crossing points along the Γ-K line, forming a nodal chain structure [45,47–49].

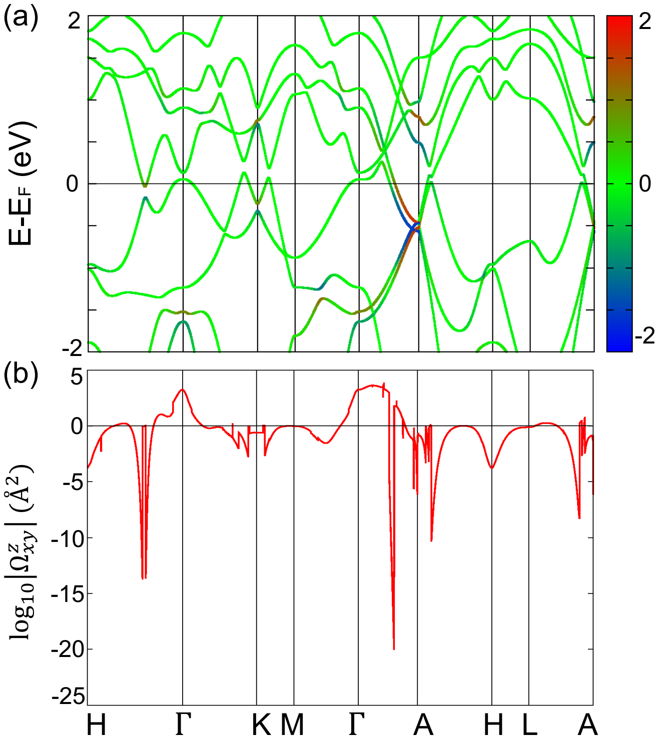

FIG. 4. (a) The band structure of ThAl$_2$ with the projection of spin Berry curvature. (b) The **k**-resolved spin Berry curvature $\Omega^z_{xy}(\mathbf{k})$ of ThAl$_2$ along the high-symmetry lines of the BZ at E_F.

Upon turning on the SOC [Fig. 2(b)], due to the inversion symmetry $\mathcal{P}$ and the time-reversal symmetry $\mathcal{T}$, the bands are all doubly degenerate, namely the Kramers degeneracy. The Kramers doublets have the opposite parities of i and $-i$ under the mirror reflection symmetry [25]. Along each high-symmetry path, the previous crossing bands near the Fermi level belong to the same irreducible representations [Fig. 2(b)]. Thus, when the SOC is included, the nodal rings on the mirror planes are all gapped [50] [Fig. 2(b)] and only extra crystalline symmetries such as glide mirror symmetry can protect a four-band-crossing nodal line in the three-dimensional system [45]. The straight nodal line along the Γ-A path is also gapped and splits into two doubly-degenerate bands, which belong to the two-dimensional irreducible representations Γ_7 and Γ_9 of the $\mathcal{C}_{6v}$ double point group, respectively. More importantly, the Fermi level locates almost within these unprotected band gaps. This is promising to induce a large SBC and then a strong SHC, because the intrinsic SHC is given by integrating the SBC of all the occupied bands in the whole BZ [Eq. (1)] and the signs of the SBC are opposite on the two bands above and below the band gap [27].

In order to investigate the relationship between the nodal lines and the SBC, we have calculated the **k**-resolved SBC at the Fermi level. Figure 3 shows the nodal lines and the corresponding distributions of the SBC in the $k_z = 0$, $k_z = \pi$, and $k_x = 0$ planes. From the figures we can see that the hot

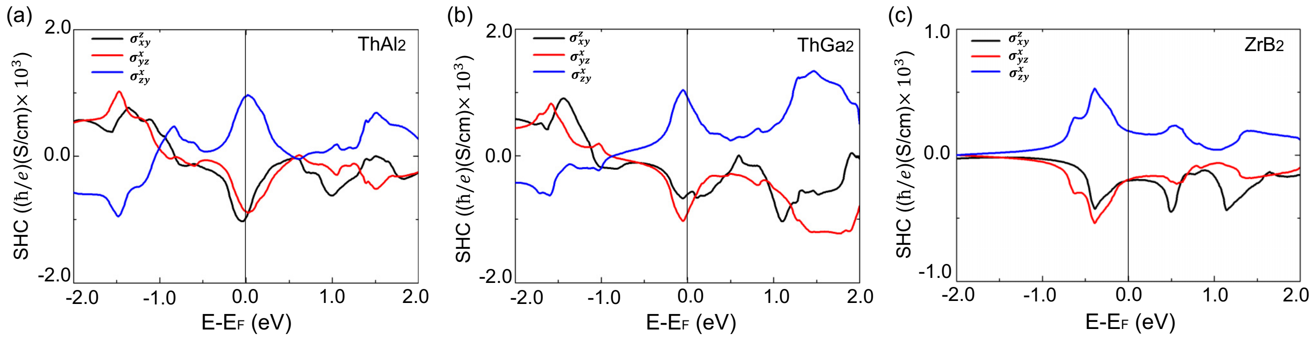

FIG. 5. Calculated spin Hall conductivity tensor elements σ^z_{xy} (black line), σ^x_{yz} (red line), σ^x_{zy} (blue line) as a function of energy for (a) $ThAl_2$, (b) $ThGa_2$, and (c) ZrB_2.

peaks of SBC appear along the original nodal lines. Since the SBC is strongly dependent on the location of the Fermi level, the magnitude of SBC in the $k_x = 0$ [Fig. 3(f)] plane is much larger than that in the $k_z = 0$ [Fig. 3(b)] and $k_z = \pi$ [Fig. 3(d)] planes. Furthermore, we have evaluated the band-projected SBC $\Omega^z_{n,xy}(\mathbf{k})$ [Eq. (3) and Fig. 4(a)] and **k**-resolved SBC $\Omega^z_{xy}(\mathbf{k})$ [Eq. (2)] along the high-symmetry paths at the Fermi energy [Fig. 4(b)], respectively. As expected, the large peaks of SBC at E_F just locate at the gapped nodal lines formed by the valence and conduction bands.

Considering that the large local SBCs are created by the gapped nodal lines, we have then computed the intrinsic SHCs of $ThAl_2$ and the isostructural $ThGa_2$ based on Eq. (1). Although the AlB_2-type $ThGa_2$ has not been synthesized experimentally [51], our phonon calculations indicate that it is dynamically stable. The nonzero elements of SHC tensor are constrained by the crystal symmetry. According to the symmetry analysis [26,52], the SHC tensor has three independent components $\sigma^z_{xy} = -\sigma^z_{yx}$, $\sigma^x_{yz} = -\sigma^y_{xz}$, and $\sigma^x_{zy} = -\sigma^y_{zx}$. Figure 5(a) and 5(b) show the energy-dependent SHC tensors of $ThAl_2$ and $ThGa_2$, respectively. It is obvious that the three elements σ^z_{xy}, σ^x_{yz}, and σ^x_{zy} all have large values in the vicinity of the Fermi energy due to the large SBC around the opened nodal-line gaps. Taking σ^x_{zy} (blue line) as an example, the values of SHC at the Fermi level reach $944\hbar/\mathrm{e}$ and $922\hbar/\mathrm{e}$ (S/cm) for $ThAl_2$ and $ThGa_2$, respectively. The σ^z_{xy} is the maximum element with $-968\hbar/\mathrm{e}$ (S/cm) at E_F and can reach $-1027\hbar/\mathrm{e}$ (S/cm) with ~0.03 hole doping for $ThAl_2$. The SHC value of $ThAl_2$ is smaller than that of the heavy metal Pt [$2000\hbar/\mathrm{e}$ (S/cm)] [10,18], but is comparable to that of β-W [$-1255\hbar/\mathrm{e}$ (S/cm)] [13]. For comparison, we have also studied the intrinsic SHCs of HfB_2 and ZrB_2, which have the same AlB_2-type structures and have been reported to host topological band features [47–49,53]. In ZrB_2 and HfB_2, the major orbitals around the Fermi level are Zr 4*d* orbitals and Hf 5*d* orbitals, while in $ThAl_2$ and $ThGa_2$, they are 6*d* and 5*f* orbitals of Th atoms. The SOC strength increases from the 4*d* (5*d*) orbitals of ZrB_2 (HfB_2) to the 6*d* and 5*f* orbitals of $ThAl_2$ and $ThGa_2$. Accordantly, the calculated maximum values of SHCs (Table I) are $-202\hbar/e$ for ZrB_2, $-522\hbar/e$ for HfB_2, $-968\hbar/e$ for $ThAl_2$, and 922 $\hbar/e$ for $ThGa_2$, respectively, which generally increase with the SOC strength of the major orbitals around the Fermi level. From ZrB_2 to $ThAl_2$, there are more anticrossing points crossing the Fermi level, leading to a larger SBC in the BZ.

We have also studied the spin Hall angle of the $ThAl_2$ system. The maximum of SHA is defined as [12],

$$\Theta_{\max} = \max\left(\frac{2e}{\hbar}\left|\frac{\sigma^k_{ij}}{\sigma_{jj}}\right|\right), \qquad (6)$$

where σ^k_{ij} is the transverse spin Hall conductivity and σ_{jj} is the longitudinal electric conductivity. According to the experimental resistivity value of 105 $\mu\Omega$ for $ThAl_2$ [34], we obtained the corresponding room-temperature relaxation time as 13.32 fs by using the Boltzmann transport equation [43]. In addition, we assumed that the relaxation time for $ThGa_2$ is equal to that of $ThAl_2$. The relatively small electrical conductivity and the large SHC in $ThAl_2$ and $ThGa_2$ will lead to a large SHA. As shown in Table I, the SHA for σ_{yz}/σ_{zz} can reach high values of 0.24 and 0.16 for $ThAl_2$ and $ThGa_2$, respectively, which are much larger than that of the heavy metal Pt (0.068) [19] and are comparable to that of β-Ta (0.15) [5]. Our theoretical results on $ThAl_2$ and $ThGa_2$ need to be confirmed by future experiments.

IV. DISCUSSION AND SUMMARY

Based on our calculations, $ThAl_2$ and $ThGa_2$ are a new class of nodal-line semimetals with large intrinsic spin Hall effect. In previous studies, several kinds of topological materials with large SHC and SHA have been investigated, which include TaAs ($-781\hbar/\mathrm{e}$) [20], TaP ($-603\hbar/\mathrm{e}$) [20], Ta_3Sb ($-1400\hbar/\mathrm{e}$) [27], HfCuGeAs ($-514\hbar/\mathrm{e}$) [30], OsO_2 ($-541\hbar/\mathrm{e}$) [25], ZrSiTe ($-755\hbar/\mathrm{e}$, 0.14) [29], ThH_2 ($1037\hbar/\mathrm{e}$, 0.23) [31], $MoTe_2$ ($29\hbar/\mathrm{e}$, 0.032) [54], WTe_2 (20-$300\hbar/\mathrm{e}$, 0.09-0.5) [55], LaAlSi ($-336\hbar/\mathrm{e}$, 0.04), and LaAlGe ($-351\hbar/\mathrm{e}$, 0.06) [32], etc. In comparison, the respective

TABLE I. Calculated nonzero spin Hall conductivity (SHC) tensor elements at the Fermi level in units of $\hbar/e$ (S/cm), the electric conductivities in units of S/cm, and the maxima of dimensionless spin Hall angles for $ThAl_2$, $ThGa_2$, HfB_2, and ZrB_2.

	σ^z_{xy}	σ^x_{yz}	σ^x_{zy}	σ_{xx}	σ_{yy}	σ_{zz}	$\lvert\Theta_{\max}\rvert$
$ThAl_2$	−968	−871	944	9524	9524	7373	0.24
$ThGa_2$	−605	−903	922	17439	17439	10974	0.16
HfB_2	−522	−512	510	66667	66667	54450	0.019
ZrB_2	−202	−194	193	25000	25000	22088	0.017

maximum values of SHC for $ThAl_2$ and $ThGa_2$ reach $-968\hbar/e$ and $922\hbar/e$ at the Fermi level, which are higher than most of above materials. Meanwhile, the three elements σ^z_{xy}, σ^x_{yz}, and σ^x_{zy} for $ThAl_2$ and $ThGa_2$ all have large values at the Fermi level, which facilitates the experimental detection of their SHE. In addition, the relatively higher values of SHA for $ThAl_2$ (0.24) and $ThGa_2$ (0.16) indicate the high efficiency of charge-spin current conversion, which offers a great advantage for their applications in spin Hall devices. Furthermore, the large spin Berry curvature induced by the multiple nodal-line gaps may also give rise to a large spin Nernst effect in $ThAl_2$ and $ThGa_2$ [30].

In summary, we have studied the intrinsic spin Hall effect in the nodal-line semimetals $ThAl_2$ and $ThGa_2$ by using first-principles electronic structure calculations. In the absence of SOC, the two compounds host multiple spinless nodal lines on the mirror planes, which form a nodal chain structure. Due to the strong SOC of Th atoms, those crossing points along the nodal lines are gapped and then induce strong spin Berry curvature and large intrinsic SHC. Considering the small electric conductivity, high SHAs can also be realized in $ThAl_2$ and $ThGa_2$. Our theoretical studies on $ThAl_2$ and $ThGa_2$ not only demonstrate the interplay between the intrinsic SHE and the band topology, but also provide a promising material platform for future application of spintronic devices.

ACKNOWLEDGMENTS

We thank P. J. Guo for helpful conversations. This work was supported by the National Key R&D Program of China (Grants No. 2017YFA0302903 and No. 2019YFA0308603), the Beijing Natural Science Foundation (Grant No. Z200005), the National Natural Science Foundation of China (Grants No. 11774424, No. 11934020, and No. 12174443), the Fundamental Research Funds for the Central Universities, and the Research Funds of Renmin University of China (Grants No. 19XNLG13 and No. 20XNH064). N.-N.Z. was supported by the Outstanding Innovative Talents Cultivation Funded Programs 2020 of Renmin University of China. Computational resources were provided by the Physical Laboratory of High Performance Computing at Renmin University of China.

---

[1] J. E. Hirsch, Phys. Rev. Lett. **83**, 1834 (1999).
[2] J. Sinova, S. O. Valenzuela, J. Wunderlich, C. H. Back, and T. Jungwirth, Rev. Mod. Phys. **87**, 1213 (2015).
[3] N. Nagaosa, J. Sinova, S. Onoda, A. H. MacDonald, and N. P. Ong, Rev. Mod. Phys. **82**, 1539 (2010).
[4] D.-F. Shao, G. Gurung, S.-H. Zhang, and E. Y. Tsymbal, Phys. Rev. Lett. **122**, 077203 (2019).
[5] L. Liu, C.-F. Pai, Y. Li, H. Tseng, D. Ralph, and R. Buhrman, Science **336**, 555 (2012).
[6] A. Manchon, J. Železný, I. M. Miron, T. Jungwirth, J. Sinova, A. Thiaville, K. Garello, and P. Gambardella, Rev. Mod. Phys. **91**, 035004 (2019).
[7] J. Sinova, D. Culcer, Q. Niu, N. A. Sinitsyn, T. Jungwirth, and A. H. MacDonald, Phys. Rev. Lett. **92**, 126603 (2004).
[8] A. Hoffmann, IEEE Trans. Magn. **49**, 5172 (2013).
[9] G.-Y. Guo, Y. Yao, and Q. Niu, Phys. Rev. Lett. **94**, 226601 (2005).
[10] G.-Y. Guo, S. Murakami, T.-W. Chen, and N. Nagaosa, Phys. Rev. Lett. **100**, 096401 (2008).
[11] W. Feng, C.-C. Liu, G.-B. Liu, J.-J. Zhou, and Y. Yao, Comput. Mater. Sci. **112**, 428 (2016).
[12] J. Qiao, J. Zhou, Z. Yuan, and W. Zhao, Phys. Rev. B **98**, 214402 (2018).
[13] X. Sui, C. Wang, J. Kim, J. Wang, S. H. Rhim, W. Duan, and N. Kioussis, Phys. Rev. B **96**, 241105(R) (2017).
[14] Y. Wang, P. Deorani, K. Banerjee, N. Koirala, M. Brahlek, S. Oh, and H. Yang, Phys. Rev. Lett. **114**, 257202 (2015).
[15] A. R. Mellnik, J. S. Lee, A. Richardella, J. L. Grab, P. J. Mintun, M. H. Fischer, A. Vaezi, A. Manchon, E.-A. Kim, N. Samarth, and D. C. Ralph, Nature (London) **511**, 449 (2014).
[16] Y. Shiomi, K. Nomura, Y. Kajiwara, K. Eto, M. Novak, K. Segawa, Y. Ando, and E. Saitoh, Phys. Rev. Lett. **113**, 196601 (2014).
[17] S. M. Farzaneh and S. Rakheja, Phys. Rev. Materials **4**, 114202 (2020).
[18] T. Kimura, Y. Otani, T. Sato, S. Takahashi, and S. Maekawa, Phys. Rev. Lett. **98**, 156601 (2007).
[19] Y. Wang, P. Deorani, X. Qiu, J. H. Kwon, and H. Yang, Appl. Phys. Lett. **105**, 152412 (2014).
[20] Y. Sun, Y. Zhang, C. Felser, and B. Yan, Phys. Rev. Lett. **117**, 146403 (2016).
[21] R. González-Hernández, E. Tuiran, and B. Uribe, Phys. Rev. Materials **4**, 124203 (2020).
[22] Y. Zhang, Q. Xu, K. Koepernik, R. Rezaev, O. Janson, J. Železný, T. Jungwirth, T. Jungwirth, C. Felser, J. van den Brink, and Y. Sun, npj Comput. Mater. **7**, 167 (2021).
[23] N.-N. Zhao, K. Liu, and Z.-Y. Lu, Phys. Rev. B **103**, 205104 (2021).
[24] Q. Wang, Y. Xu, R. Lou, Z. Liu, M. Li, Y. Huang, D. Shen, H. Weng, S. Wang, and H. Lei, Nat. Commun. **9**, 3681 (2018).
[25] Y. Sun, Y. Zhang, C.-X. Liu, C. Felser, and B. Yan, Phys. Rev. B **95**, 235104 (2017).
[26] S. Bhowal and S. Satpathy, Phys. Rev. B **100**, 115101 (2019).
[27] E. Derunova, Y. Sun, C. Felser, S. S. P. Parkin, B. Yan, and M. N. Ali, Sci. Adv. **5**, eaav8575 (2019).
[28] W. Hou, J. Liu, X. Zuo, J. Xu, X. Zhang, D. Liu, M. Zhao, Z.-G. Zhu, H.-G. Luo, and W. Zhao, npj Comput. Mater. **7**, 37 (2021).
[29] Y. Yen and G.-Y. Guo, Phys. Rev. B **101**, 064430 (2020).
[30] B. B. Prasad and G.-Y. Guo, Phys. Rev. Materials **4**, 124205 (2020).
[31] X. Zuo, Q. Gao, X. Sui, X. Xu, X. Jiang, L. Han, H. Li, D. Li, D. Liu, B. Huang, and B. Cui, Phys. Rev. B **103**, 125159 (2021).
[32] T. Ng, Y. Luo, J. Yuan, Y. Wu, H. Yang, and L. Shen, Phys. Rev. B **104**, 014412 (2021).
[33] J. Zhou, J. Qiao, A. Bournel, and W. Zhao, Phys. Rev. B **99**, 060408(R) (2019).

[34] M. Sekar, N. V. Chandra Shekar, P. Ch. Sahu and K. Govinda Rajan, J. Alloys Compd. **350**, 1 (2003).

[35] P. Hohenberg and W. Kohn, Phys. Rev. **136**, B864 (1964).

[36] W. Kohn and L. J. Sham, Phys. Rev. **140**, A1133 (1965).

[37] P. Giannozzi, S. Baroni, N. Bonini, M. Calandra, R. Car, C. Cavazzoni, D. Ceresoli, G. L. Chiarotti, M. Cococcioni, I. Dabo *et al.*, J. Phys.: Condens. Matter **21**, 395502 (2009).

[38] A. Dal Corso, Comput. Mater. Sci. **95**, 337 (2014).

[39] https://www.quantum-espresso.org/pseudopotentials.

[40] J. P. Perdew, K. Burke, and M. Ernzerhof, Phys. Rev. Lett. **77**, 3865 (1996).

[41] N. Marzari, A. A. Mostofi, J. R. Yates, I. Souza, and D. Vanderbilt, Rev. Mod. Phys. **84**, 1419 (2012).

[42] A. A. Mostofi, J. R. Yates, G. Pizzi, Y.-S. Lee, I. Souza, D. Vanderbilt, and N. Marzari, Comput. Phys. Commun. **185**, 2309 (2014).

[43] G. Pizzi, D. Volja, B. Kozinsky, M. Fornari, and N. Marzari, Comput. Phys. Commun. **185**, 422 (2014).

[44] A. Brown, Acta Crystallogr. **14**, 860 (1961).

[45] C. Fang, Y. Chen, H.-Y. Kee, and L. Fu, Phys. Rev. B **92**, 081201(R) (2015).

[46] J. Wang, Y. Liu, K.-H. Jin, X. Sui, L. Zhang, W. Duan, F. Liu, and B. Huang, Phys. Rev. B **98**, 201112(R) (2018).

[47] C.-J. Yi, B. Q. Lv, Q. S. Wu, B.-B. Fu, X. Gao, M. Yang, X.-L. Peng, M. Li, Y.-B. Huang, P. Richard, M. Shi, G. Li, Oleg V. Yazyev, Y.-G. Shi, T. Qian, and H. Ding, Phys. Rev. B **97**, 201107(R) (2018).

[48] X. Feng, C. Yue, Z. Song, Q. S. Wu, and B. Wen, Phys. Rev. Materials **2**, 014202 (2018).

[49] R. Lou, P. Guo, M. Li, Q. Wang, Z. Liu, S. Sun, C. Li, X. Wu, Z. Wang, Z. Sun, D. Shen, Y. Huang, K. Liu, Z.-Y. Lu, H. Lei, H. Ding, and S. Wang, npj Quantum Mater. **3**, 43 (2018).

[50] R. González-Hernández, E. Tuiran and B. Uribe, Phys. Rev. B **104**, 205128 (2021).

[51] N. V. Chandra Shekar, N. R. Sanjay Kumar, M. Sekar, P. Ch. Sahu, K. Govinda Rajan, Philos. Mag. Lett. **83**, 333 (2003).

[52] M. Seemann, D. Kodderitzsch, S. Wimmer, and H. Ebert, Phys. Rev. B **92**, 155138 (2015).

[53] X. Zhang, Z.-M. Yu, X.-L. Sheng, H. Y. Yang, and S. A. Yang, Phys. Rev. B **95**, 235116 (2017).

[54] G. M. Stiehl, R. Li, V. Gupta, I. E. Baggari, S. Jiang, H. Xie, L. F. Kourkoutis, K. F. Mak, J. Shan, R. A. Buhrman, and D. Ralph, Phys. Rev. B **100**, 184402 (2019).

[55] D. MacNeill, G. Stiehl, M. Guimaraes, R. Buhrman, J. Park, and D. Ralph, Nat. Phys. **13**, 300 (2017).